ROYAL SOCIETY
OF CHEMISTRY

PAPER

Check for updates

Magnetically recoverable MFe$_{12}$O$_{19}$ nanoparticles as efficient and environmentally benign catalysts for gram-scale selective oxidation of olefins

Mouhsine Laayati,[abe] Ayoub Abdelkader Mekkaoui, [ID] *[b] Ahsen Sare Yalın,[c] Abdelhamid El Boubekri,[d] Mohammed Sajieddine,[d] Larbi El Firdoussi,[b] Antonia Neels, [ID] [e] Önder Metin [ID] [cf] and Soufiane El Houssame [ID] *[a]

Catalytic oxidation is an efficient route for synthesizing oxygenated compounds such as epoxides and aldehydes. However, developing cost-effective, environmentally friendly and selective gram-scale catalysts, in full agreement with circular economy and green chemistry principles, remains a significant challenge. Herein, we report on MFe$_{12}$O$_{19}$ magnetic nanoparticles (MNPs) as a novel, magnetically recoverable and selective catalyst for the oxidation of olefins. Three different MFe$_{12}$O$_{19}$ (M = Cu, Sn and Sr) MNPs were synthesized using the coprecipitation method and characterized by XRD, FTIR, Raman, XPS, SEM-EDX, TEM, BET, zeta potential and ^{57}Fe Mössbauer spectroscopy. XRD analysis demonstrates that the patterns of SnFe$_{12}$O$_{19}$ and CuFe$_{12}$O$_{19}$ are totally different from those of the magnetoplumbite hexaferrite structure due to the confirmed coexistence by Rietveld refinements of SnO$_2$−Fe$_2$O$_3$ and CuFe$_2$O$_4$−Fe$_2$O$_3$ as composite structures, respectively. In good agreement, Raman studies exclusively confirms the coexistence of MO$_x$−Fe$_2$O$_3$ as a composite structure in MFe$_{12}$O$_{19}$, due to the presence of α-Fe$_2$O$_3$ and γ-Fe$_2$O$_3$ as intermediate phases during the formation process of the hexaferrite structure. Moreover, the XPS and Mössbauer results are consistent with the experimental evidence and spectroscopic characterizations. Subsequently, the catalytic activity of the as-synthesized MNPs was evaluated for the oxidation of styrene as a model olefinic substrate. Among the as-prepared MFe$_{12}$O$_{19}$ MNPs, the composite structure CuFe$_2$O$_4$−Fe$_2$O$_3$ in CuFe$_{12}$O$_{19}$ effectively enhances catalytic activity, selectivity and reusability due to the synergistic catalytic effect within a single magnetically recoverable nanostructure. Overall, MFe$_{12}$O$_{19}$ MNPs present a facile and greener approach using magnetically recyclable hexaferrites for selective catalytic oxidation reactions.

1. Introduction

Styrene oxide and benzaldehyde are important organic intermediates widely used in the industrial manufacture of fragrances, pharmaceuticals, and organic synthesis.[1–4] Hence, the oxidation of olefins has been widely regarded as one of the most important routes to accessing epoxides and aldehydes.[5] To date, both homogeneous and heterogeneous catalysts have been extensively reported for the oxidation of olefins.[6–15] Catalysis plays an important role in green chemistry by enabling less polluting chemical processes and providing sustainable pathways to synthesize desired products.[16] Heterogeneous catalysts are widely preferred over homogeneous ones owing to their recyclability and atom economy, which contribute to sustainability by reducing time- and energy-consuming catalytic processes in alignment with the circular economy. Particular attention has been given to the development of selective heterogenous catalysts for the oxidation of styrene to benzaldehyde or styrene oxide. Magnetic nanoparticles (MNPs) are especially attractive candidates for this reaction owing to their high activity, selectivity, and facile reusability.[17] Moreover, MNPs exhibit numerous advantageous properties, including a large surface-to-volume ratio, good crystallinity, excellent thermal stability and homogeneous composition as heterogeneous bulk catalysts, all of which contribute to their high catalytic performance.[17–20]

[a]*Laboratoire des Sciences des Matériaux, Mathématiques et Environnement, Université Sultan Moulay Slimane, Faculté Polydisciplinaire de Khouribga, BP 145, Khouribga 25000, Morocco. E-mail: hous_soufiane@hotmail.com*

[b]*Cadi Ayyad University, UCA, Faculté des Sciences Semlalia Marrakech, Département de Chimie, Laboratoire de Chimie Moléculaire, Equipe de Chimie de Coordination et de Catalyse, BP 2390, Marrakech 40001, Morocco. E-mail: mekk.ayoub@gmail.com; a. mekkaoui@uca.ac.ma*

[c]*Department of Chemistry, College of Sciences, Koç University, 34450 Istanbul, Turkey*

[d]*Laboratoire Génie Energétique et Matériaux, Université Sultan Moulay Slimane, Faculté des Sciences et Techniques, BP 523, Béni Mellal 23000, Morocco*

[e]*Center for X-Ray Analytics, Empa - Swiss Federal Laboratories for Materials Science and Technology, Überlandstrasse 129, 8600 Dübendorf, Switzerland*

[f]*Koç University Surface Science and Technology Center (KUYTAM), Koç University, Istanbul 34450, Turkey*

M-type hexaferrite, with a chemical formula of $MFe_{12}O_{19}$, is a class of promising chemically and thermally stable magnetic materials for a wide range of applications. Regarding their high magneto-crystalline anisotropy with a single easy magnetization axis, they are classified as hard magnets with high coercivity.[21] They have been widely used as permanent magnets, recording media, photocatalysts and components in microwave, tele-communication, higher-frequency, and magnetooptical devices.[22-29] Moreover, special attention has been given to magnetic materials based on barium, strontium, palladium and lead with unique properties.[30] Previously, Ansari et al. reported on the synthesis of $CuFe_{12}O_{19}$ nanostructures by using sol–gel auto-combustion method and its magnetic properties.[31] Recently, $SnFe_{12}O_{19}$ nanostructures were synthesized through ultrasonic irradiation and utilized in an environmental application.[32] Based on the current understanding, the XRD patterns of these reported structures $MFe_{12}O_{19}$ (M = Cu or Sn) are not yet confirmed, and they are totally different from those of the magnetoplumbite hexaferrite structure. Hence, there is a lack of advanced spectroscopic investigations in the reported literature to accurately assess the structural properties of such $MFe_{12}O_{19}$ compounds. For this reason, Cu and Sn have been selected to study the obtained $MFe_{12}O_{19}$ compounds and compare them with the $SrFe_{12}O_{19}$ M-type hexaferrite.

In the last decades, owing to their magnetic properties, M-type hexaferrites have attracted the attention of scientists in various fields of catalytic applications. Recently, the $SrFe_{12}O_{19}$ M-type hexaferrite was reported as high catalytically active MNPs for the improvement of the catalytic epoxide ring-opening reaction with amines, as pristine[33] or in hybrid graphene-derived nanocomposites,[34] as well as in the synthesis of 2-amino-4,6-diphenylnicotinonitrile[35] and 1,5-benzodiaze-pine derivatives.[36] However, the presumed $MFe_{12}O_{19}$ (M = Cu or Sn) nanoparticles have only been reported in a few studies. According to the literature, $CuFe_{12}O_{19}$ MNPs and the grafted ones on CNT have only been reported for photocatalytic elimination of water contamination.[37,38] To the best of our knowledge, $CuFe_{12}O_{19}$ and $SnFe_{12}O_{19}$ nanoparticles have not yet been used as heterogeneous catalysts for any application. In this regard, the growing potential of hexaferrite MNPs in catalysis motivates further study of their catalytic activity in alignment with green chemistry principles and circular economy.

In this study, we focus on the development of novel hex-aferrite nanostructures as magnetically recoverable nano-particles (MNPs) for catalytic applications, leveraging their magnetic properties, stability and high specific surface area. Various chemical methods, including sol–gel,[31,39,40] salt melting process,[41] sonochemical[32,42] and coprecipitation,[33,43] have previously been employed for the synthesis of M-type hex-aferrites. Among these, the chemical coprecipitation method stands out due to its simplicity and precision in controlling the grain size, making it an excellent approach for preparing magnetic oxide nanoparticles. Herein, we present the synthesis of $CuFe_{12}O_{19}$, $SnFe_{12}O_{19}$ and $SrFe_{12}O_{19}$ NPs using a reproducible coprecipitation method. To the best of our knowledge, this is the first study to evaluate the catalytic performance of as-prepared $MFe_{12}O_{19}$ NPs in the oxidation of styrene derivatives, chosen as model substrates for olefin oxidation.

2. Experimental

2.1. Materials

All reagents and solvents were obtained from commercial suppliers (Aldrich and Acros), and used directly without further purification. As-synthesized nanoparticles (NPs) were characterized by X'Pert MPD Powder instrument from Malvern Pan-alytical with Cu Kα radiation (λ_{Cu} = 1.5406 Å). A Bruker vertex 70 DTGSFTIR spectrophotometer was used to record the stretching vibrational frequencies of NPs in the range of 400–4000 cm^{-1}. X-ray photoelectron spectra (XPS) were obtained using a Thermo Scientific K-Alpha spectrometer using an aluminum anode (Al K$\alpha_{1/4}$ 1468.3 eV). The binding energies were calibrated by referencing the C 1s signal at 284.4 eV. Morphology and topology of the materials were characterized by using a scanning electron microscope (SEM) (FEI, Quanta FEG 450). Transmission Mössbauer spectra were collected by using a conventional constant acceleration spectrometer with a 25 mCi source ^{57}Co sealed in a Rh matrix at room temperature. In this configuration, the γ-ray direction is perpendicular to the powder plane. NORMOS DIST program was used to interpret the experimental spectra.[44] All isomer shift values are reported with respect to that of the α-iron foil at room temperature. Transmission electron microscope (TEM) images were recorded on a 120 kV Hitachi HT7800 TEM instrument with EXALENS module capable of working at high-resolution (HR) mode in the magnification range of 10–600k×. BET measurements were conducted using the Micromeritics Tristar II automated gas sorption system. The zeta potential was measured using a Malvern Panalytical Zetasizer, after dispersing 0.1 g of nanopowders in 3 ml of solvent (acetonitrile; acetone or deionized water). Aliquot samples from the reaction mixture were monitored by gas chromatography (GC, Shimadzu) equipped with a flame ionization detector and nitrogen as the carrier gas. The GC conditions for the BP capillary columns (25 m × 0.25 mm, SGE) were set as follows: injector temperature at 250 °C; detector temperature at 250 °C and oven temperature initially set at 70 °C for 5 min, followed by a ramp of 3 °C min^{-1} until reaching 250 °C for 30 min. The column pressure was maintained at 20 kPa with a flow rate of 6.3 ml min^{-1}, linear velocity of 53.1 cm s^{-1} and total flow of 138 ml min^{-1}. The products were confirmed by injecting the reaction mixture into an ISQ LT single quadrupole mass spectrometer, operating in positive EI mode, and scannig a mass range of 50 to 400 m/z.

2.2. Synthesis of the $MFe_{12}O_{19}$ nanoparticles

The magnetic $MFe_{12}O_{19}$ (M = Sr; Cu; or Sn) nanoparticles were synthesized by following a coprecipitation protocol.[33,34] In a typical synthesis protocol, stoichiometric quantities of metal chlorides ($SrCl_2 \cdot 6H_2O$; $CuCl_2$; $SnCl_2 \cdot 2H_2O$; $FeCl_3$) were individually dissolved in 30 ml of deionized water to form homogeneous solutions. These solution were then mixed and stirred for 30 min at 80 °C. Next, pH of the reaction mixture was

adjusted to 11–12 *via* dropwise addition of NaOH (1.5 M) under continuous stirring for 1.5–2 h at 80 °C, ensuring the homogeneity of the mixture. The precipitated $CuFe_{12}O_{19}$ and $SnFe_{12}O_{19}$ nanopowders were separated magnetically. In contrast, $SnFe_{12}O_{19}$ was separated *via* centrifugation due to the lack of its magnetization. The prepared $MFe_{12}O_{19}$ nanopowders were washed several times with deionized water to remove the excess salt and dried at 80 °C overnight. The obtained nanopowders were calcined at 900 °C for 8 h to obtain the pure hexaferrites.

2.3. Catalytic studies

2.3.1. Selective synthesis of epoxide or aldehyde derivatives. In a typical reaction, the synthesis of epoxide derivatives was performed by combining olefin (1.92 mmol), *t*BHP 70 wt% (3 eq.), $CuFe_{12}O_{19}$ (1.92×10^{-2} mmol, %mol ($CuFe_{12}O_{19}$) = 1%) and 2 ml of acetonitrile as solvent. The mixture was then placed in a 50 ml Rotaflow tube and stirred at 60 °C for 24 h. The progress of the reaction was monitored by GC using dodecane as the internal standard. At the end of the reaction, the catalyst was recovered by an external magnetic field, washed with deionized water and acetone, and dried in an oven at 80 °C for 6 h before reuse. For the synthesis of the aldehyde derivatives, the oxidation reaction was carried out in the presence of H_2O_2, 30 wt% (3 eq.), in 2 ml of acetone as the solvent at 80 °C for 24 h.

3. Results and discussion

3.1. $MFe_{12}O_{19}$ characterization

The structures of the as-synthesized $MFe_{12}O_{19}$ NPs (M = Cu, Sn and Sr) were first characterized by X-ray diffraction (XRD) (Fig. 1). While all the diffraction lines of $CuFe_{12}O_{19}$ MNPs match the reported ones in the literature,[31] the diffraction patterns of $CuFe_2O_4$ (JCPDS: 77-0010) and Fe_2O_3 (JCPDS: 24-0072) reveal the coexistence of $CuFe_2O_4$–Fe_2O_3 as a composite structure in the as-synthesized $CuFe_{12}O_{19}$ MNPs. Accordingly, while the XRD pattern of $SnFe_{12}O_{19}$ also matched the reported literature,[32] the crystalline phases of SnO_2 (JCPDS: 72-1147) and Fe_2O_3 (JCPDS: 24-0072) indicate the coexistence of SnO_2–Fe_2O_3 as possible composite structure. However, the XRD pattern of the as-prepared $SrFe_{12}O_{19}$ presents a very similar diffraction pattern

Fig. 1 XRD patterns of $CuFe_{12}O_{19}$, $SnFe_{12}O_{19}$ and $SrFe_{12}O_{19}$.

as reported for the magnetoplumbite hexaferrite structure.[34] In addition, the $SrFe_{12}O_{19}$ crystal phase clearly matches well with the known strontium hexaferrite crystal phase (JCPDS: 33-1340). No obvious peaks of metal oxides (SrO and Fe_2O_3) are observed, clearly indicating only the presence of the pure $SrFe_{12}O_{19}$ hexaferrite structure.

Based on the XRD results, Rietveld refinement was carried out to accurately assess the observed structural differences of both compounds $CuFe_{12}O_{19}$ and $SnFe_{12}O_{19}$ compared to the magnetoplumbite M-type hexaferrite structure of the $SrFe_{12}O_{19}$ MNPs. The recorded and Rietveld refined XRD patterns of the as-presumed prepared hexaferrites are displayed in Fig. 2. Clearly, in $SnFe_{12}O_{19}$ and $CuFe_{12}O_{19}$, the refined XRD patterns exhibit a combination of two distinct parent phases. The refinement confirmed that $CuFe_{12}O_{19}$ exhibits a spinel structure with the $Fd\bar{3}m$ space group and hematite (Fe_2O_3) as the main phase (73.5%). However, the $SnFe_{12}O_{19}$ XRD pattern presents the hematite phase (92.5%) as the major component and the minor crystalline phase of SnO_2 (7.5%). Table 1 presents the fitting parameters and crystallite sizes (D), using the most intense and single indexed reflection of all phases, as found in the as-prepared $MFe_{12}O_{19}$ NPs.

The Rietveld refinement study reveals good agreement between the experimental and calculated patterns. Moreover, based on what is currently known, we can assume that the structural properties of both $CuFe_{12}O_{19}$ and $SnFe_{12}O_{19}$ have never been reported with such experimental proof, which may explain the XRD outcomes compared to the magnetoplumbite structure due to the coexistence of SnO_2–Fe_2O_3 and $CuFe_2O_4$–Fe_2O_3. Consequently, we can assume that they are not isostructural with the $SrFe_{12}O_{19}$ M-type hexaferrite.

The FTIR spectra of all synthesized $MFe_{12}O_{19}$ NPs present the characteristic peaks of metal–oxygen stretching vibrations at around 460–630 cm^{-1} (Fig. 3).[34] However, the peaks around 3400 and 1600 cm^{-1} are attributed to the stretching and the bending vibrations, respectively, of the adsorbed water on the $MFe_{12}O_{19}$ NPs.[32,38]

Fig. 4 shows the Raman spectra of the obtained $MFe_{12}O_{19}$ NPs. The Raman shifts observed for $SrFe_{12}O_{19}$ are attributed to the A_{1g}, E_{1g}, and E_{2g} modes. The tetrahedral 4f1 and bipyramidal 2b sites of $SrFe_{12}O_{19}$ exhibit A_{1g} vibrations of Fe–O bonds at 724 and 690 cm^{-1}, respectively. Meanwhile, the octahedral 4f2, 2a and 12k sites exhibit the same A_{1g} vibrations at 620 and 479 cm^{-1}, respectively. At the octahedral 12k dominant site, the peak of the A_{1g} vibrations was detected at 407 cm^{-1}. The band at 347 cm^{-1} is attributed to an octahedra mode mix with A_{1g} and E_{1g} symmetries. While the E_{1g} vibrations of the entire spinel block are shown at 185 cm^{-1}, the E_{1g} vibration modes are also seen at 295 and 225 cm^{-1}. The bands at 534 and 432 cm^{-1} were both attributed to E_{2g} modes.[45,46] On the other hand, the Raman spectrum of $SnFe_{12}O_{19}$ reveals three Raman active modes (Fig. 4). While the observed peaks at 222 and 497 cm^{-1} are both attributed to A_{1g}, the remaining four peaks at 243, 284, 407, and 609 cm^{-1} may be assigned to the E_g mode of α-Fe_2O_3 NPs.[47] However, the peaks at 499 and 701 cm^{-1} are assigned to the E_g and A_{2u} active modes of SnO_2.[47] In addition, the Raman spectrum of $CuFe_{12}O_{19}$ reveals peaks at
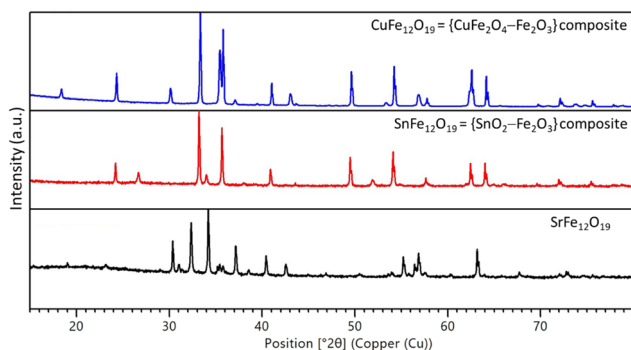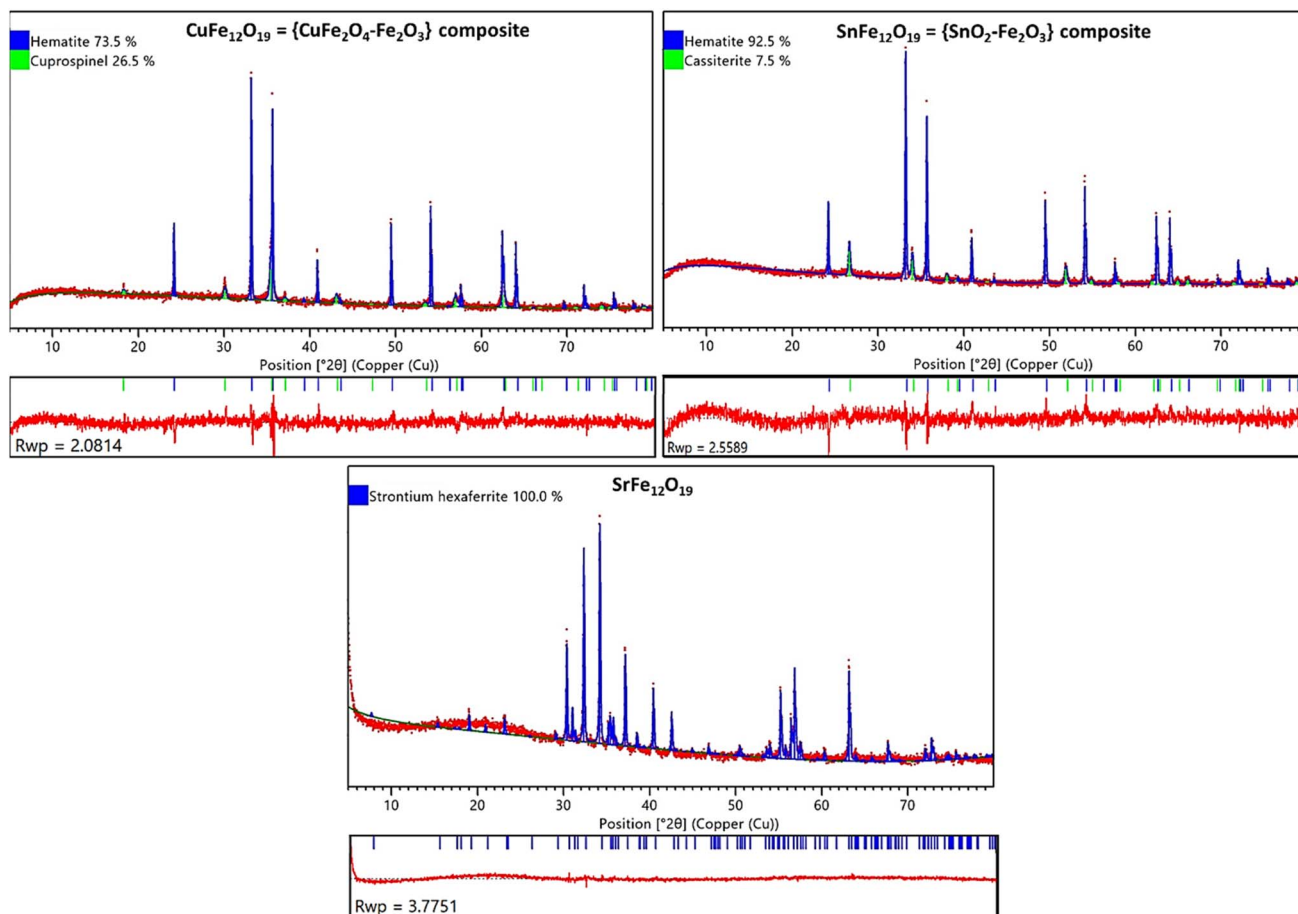
Fig. 2 Rietveld refinement of $CuFe_{12}O_{19}$, $SnFe_{12}O_{19}$ and $SrFe_{12}O_{19}$.

Table 1 Refined parameters of the XRD data for $MFe_{12}O_{19}$ (M = Cu, Sn and Sr)

	$CuFe_{12}O_{19} = \{CuFe_2O_4–Fe_2O_3\}$		$SnFe_{12}O_{19} = \{SnO_2–Fe_2O_3\}$		$SrFe_{12}O_{19}$
Phase	$CuFe_2O_4$	Fe_2O_3	SnO_2	Fe_2O_3	$SrFe_{12}O_{19}$
Crystal structure	Cubic spinel	Hexagonal	Tetragonal	Hexagonal	Hexagonal
Group space	$Fd\bar{3}m$	$R\bar{3}c$	$P4_2/mnm$	$R\bar{3}c$	$P6_3/mmc$
Composition (%)	23.8	76.2	7.5	92.5	100
a (Å)	8.42	5.033	4.735	5.037	5.882
b (Å)	8.42	5.033	4.735	5.037	5.882
c (Å)	8.42	13.741	3.179	13.748	23.051
V (Å³)	598.69	301.53	71.28	302.11	690.85
D (nm)	52.2	119.9	37.4	160.1	118.1
R_{wp} (%)	8.09		2.55		3.77
R_p (%)	4.61		1.99		2.62
R_{exp} (%)	1.77		1.93		1.61
χ^2	4.56		1.32		2.33

226, 228, 409, 611, and 656 cm^{-1}, matching the Raman active modes of α-Fe$_2$O$_3$ NPs.[48] Moreover, the broad peak around 1303 cm^{-1} observed in all samples, with a noticeable differentiation in intensity, could be attributed to the Raman mode of α-Fe$_2$O$_3$,[49] which is in good agreement with the Rietveld study. Furthermore, the significant intensity of the α-Fe$_2$O$_3$

peak in the SnFe$_{12}$O$_{19}$ structure may explain its lack of magnetization. In conclusion, the Raman spectra support the recorded and Rietveld refined XRD patterns, especially those of CuFe$_{12}$O$_{19}$ and SnFe$_{12}$O$_{19}$, about a possible coexistence of MO$_x$–Fe$_2$O$_3$ as a composite structure in the MFe$_{12}$O$_{19}$ composition. Indeed, it was reported that α-Fe$_2$O$_3$ and γ-Fe$_2$O$_3$ are
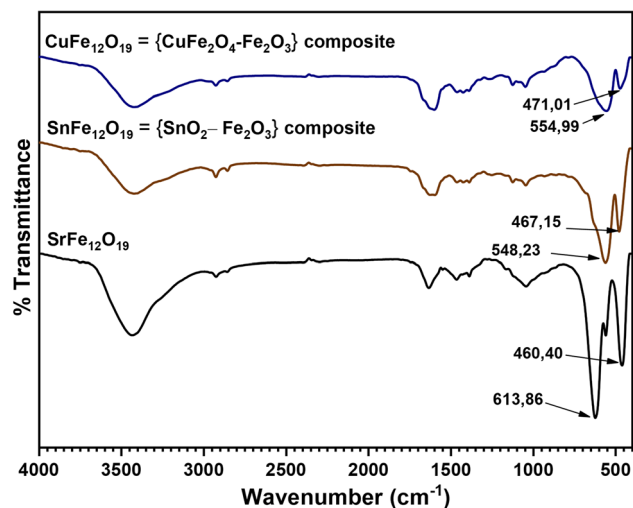
Fig. 3 FTIR spectra of $CuFe_{12}O_{19}$, $SnFe_{12}O_{19}$ and $SrFe_{12}O_{19}$.

intermediate phases during the formation process of the hexaferrite structure.[49,50] Moreover, their existence as intermediate phases supports the formation mechanism of $MFe_{12}O_{19}$. Specifically, the γ-Fe_2O_3 phase is formed at low temperatures and incorporates cations into MFe_2O_4, which further reacts with γ-Fe_2O_3 to form the $MFe_{12}O_{19}$ phase. However, the α-Fe_2O_3 phase appears at higher temperatures, accompanied by the formation of the hexaferrite structure.

To understand the surface electronic and chemical configurations of the as-synthesized $MFe_{12}O_{19}$ NPs, XPS analyses were carried out (Fig. 5). The chemical environment and the oxidation state of Cu, Sr, Sn and Fe were studied through the Cu 2p, Sr 3d, Sn 3p, Sn 3d and Fe 2p regions (Fig. 5b and c). All the expected elements, Cu, Sr, Sn, Fe and O, were detected in the XPS survey spectra of $MFe_{12}O_{19}$ (Fig. 5a_1–a_3). The high-resolution XPS spectrum of the Cu 2p region in $CuFe_{12}O_{19}$ shows the characteristic peaks of the Cu $2p_{3/2}$ and Cu $2p_{1/2}$ core-

levels at the binding energies (BEs) of 933.38 and 953.10 eV, as well as two additional peaks attributed to shakeup satellites at BEs of 940.49 and 961.78 eV (Fig. 5b_1), respectively. Deconvolution of the Cu 2p XPS spectrum indicated the presence of Cu^{2+} of $CuFe_2O_4$ in the as-synthesized $CuFe_{12}O_{19}$.[51] Meanwhile, the peaks located at BEs of 486.13 and 494.60 eV are attributed to $3d_{5/2}$ and $3d_{3/2}$ of Sn^{4+} (Fig. 5b_3), respectively. In addition, the Sn $3d_{5/2}$ and Sn $3d_{3/2}$ core-levels are presented as a doublet with a spin–orbit split of ≈ 8.5 eV, which confirms the presence of SnO_2 in the $SnFe_{12}O_{19}$ composite structure.[52] However, the XPS spectrum of Sr 3d in $SrFe_{12}O_{19}$ exhibits two peaks at BEs of 133.38 and 134.98 eV, attributed to the characteristic doublets of Sr^{2+} (Sr $3d_{5/2}$ and Sr $3d_{3/2}$, respectively) (Fig. 5b_3).[53]

The high-resolution XPS spectra of the Fe 2p regions of the $MFe_{12}O_{19}$ NPs ($CuFe_{12}O_{19}$, $SnFe_{12}O_{19}$, and $SrFe_{12}O_{19}$) show similar two spin–orbit doublets at BEs of around 710 and 720 eV, corresponding to the Fe $2p_{3/2}$ and Fe $2p_{1/2}$ core-levels, as well as two additional peaks attributed to shakeup satellites at BEs of around 719 and 732 eV (Fig. 5c), respectively. Hence, the obtained 2p peaks and satellite peaks of Fe are in close agreement with the reported values for Fe^{3+} and the energy differences between the main $2p_{3/2}$ and $2p_{1/2}$ peaks (≈ 13.5 eV), confirming the electronic state of Fe^{3+}.[54] Moreover, this electronic state in the as-synthesized $MFe_{12}O_{19}$ NPs can be assigned to the contributions from Fe^{3+} in the octahedral and tetrahedral sites.[54] However, the noticeable difference in XPS spectrum of Fe in $SnFe_{12}O_{19}$ is due to the appearance of Sn $3p_{3/2}$ at the BE of 725.61 eV, which is in the same region as the shakeup satellite (at BE of 718.98 eV).[55] The deconvoluted spectra of O 1s show two peaks in the BE region of around 529–534 eV (Fig. 5d). While the peak at BE of around 530 eV is ascribed to the lattice oxygen in the metal–oxygen bond, the other one at BE of around 531.5 eV corresponds to the adsorbed O^- or O_2^{2-} species, which are associated with the intrinsic oxygen vacancies on the surface. However, the peak at BE of 530.04 eV for $SrFe_{12}O_{19}$ is shifted to BE of around 529.5 eV in both $CuFe_{12}O_{19}$ and
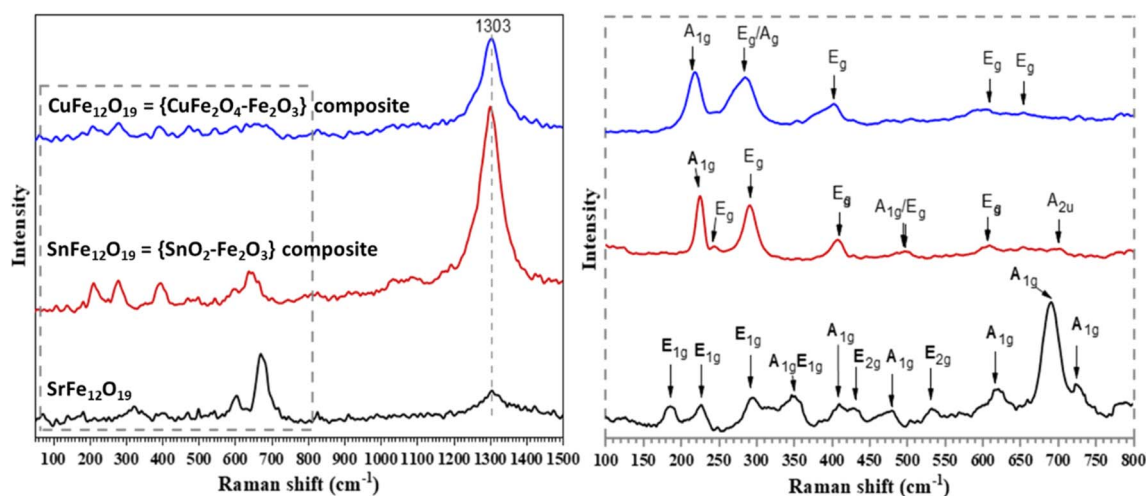

Fig. 4 Raman spectra of $CuFe_{12}O_{19}$, $SnFe_{12}O_{19}$ and $SrFe_{12}O_{19}$.
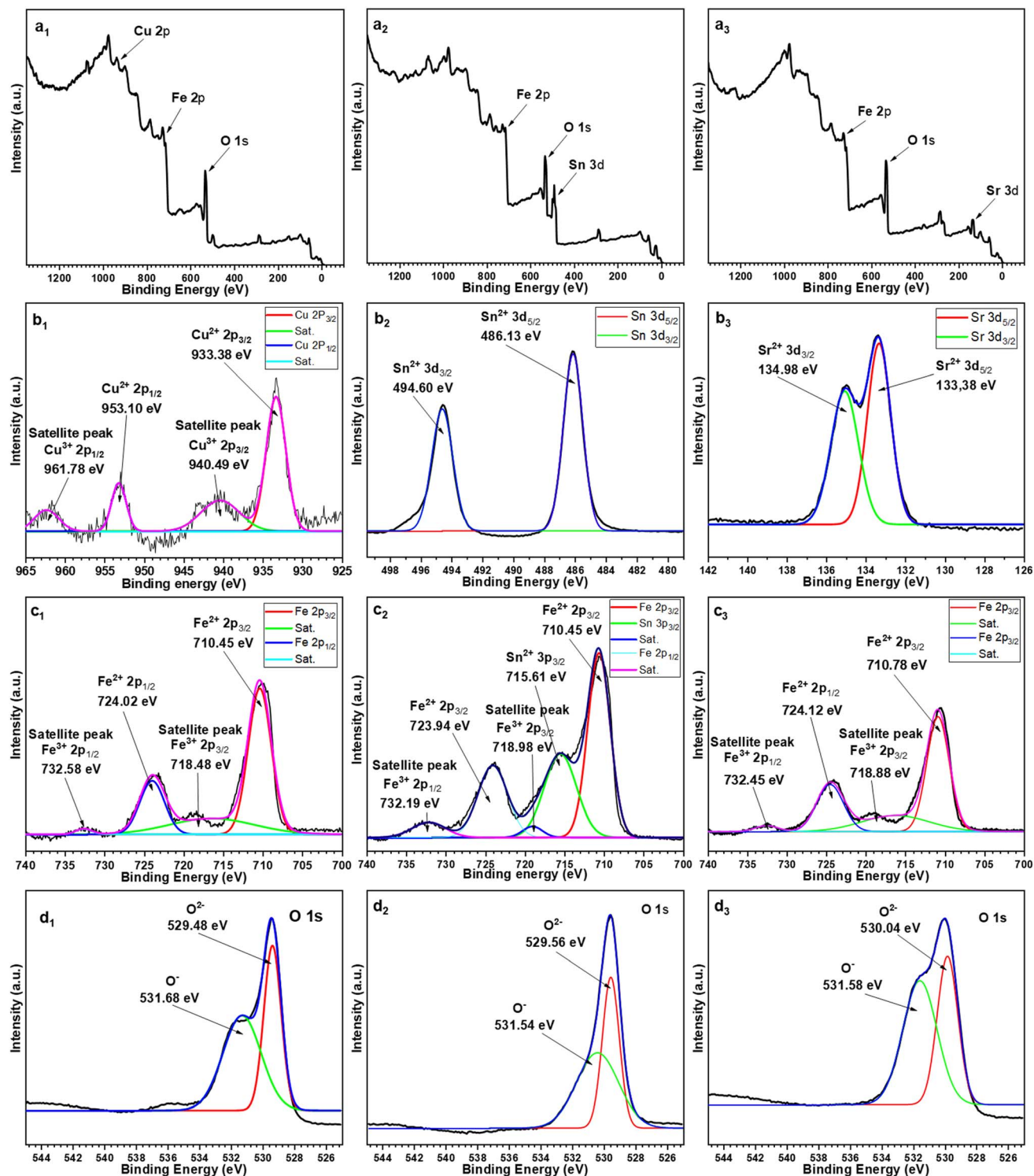
Fig. 5 XPS survey ($a_{1–3}$), high-resolution M (M = Cu 2p, Sr 3d, and Sn 3d) ($b_{1–3}$), Fe 2p ($c_{1–3}$) and O 1s spectra ($d_{1–3}$) of $CuFe_{12}O_{19}$, $SnFe_{12}O_{19}$, and $SrFe_{12}O_{19}$, respectively.

$SnFe_{12}O_{19}$, which could be attributed to the characteristic peak of O^{2-} in the hybrid oxide framework.[56]

^{57}Fe Mössbauer spectroscopy is a highly effective technique for examining the oxidation state, local environment and magnetic characteristics of Fe atoms in the studied $MFe_{12}O_{19}$ NPs. Fig. 6 shows the room temperature Mössbauer spectra of $CuFe_{12}O_{19}$, $SnFe_{12}O_{19}$ and $SrFe_{12}O_{19}$ NPs. For $CuFe_{12}O_{19}$, the Mössbauer spectrum is well fitted using two sextets and one doublet, which confirms the presence of the $CuFe_2O_4$–Fe_2O_3 composite structure. While the two sextets are characteristic of
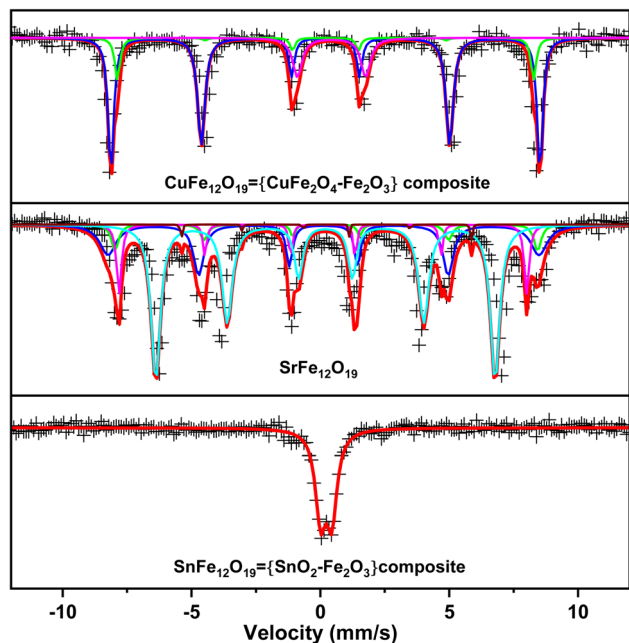
Fig. 6 ^{57}Fe Mössbauer spectra recorded at room temperature of $CuFe_{12}O_{19}$, $SnFe_{12}O_{19}$ and $SrFe_{12}O_{19}$.

the A and B sites of the Fe^{3+} ions present in the magnetically ordered structure of $CuFe_2O_4$ at the tetrahedral and octahedral sites, the doublet is associated with Fe^{3+} ions in the paramagnetic state of α-Fe_2O_3. However, the fitted experimental spectrum of $SrFe_{12}O_{19}$ reveals a superposition of five magnetically split spectral components (sextets) characteristic of five different atomic environments around the Fe nuclei in the $SrFe_{12}O_{19}$ M-type hexaferrite structure. Each one of these sextets is associated with a specific Fe^{3+} crystallographic site: one tetrahedral (4f1), one bipyramidal (2b) and three octahedral sites (12k, 4f2, and 2a). On the other hand, the spectrum of $SnFe_{12}O_{19}$ shows a doublet characteristic of the paramagnetic iron atoms, confirming the lack of magnetization of the as-synthesized $SnFe_{12}O_{19}$ nanoparticles due to the presence of the SnO_2–Fe_2O_3 composite structure. Table 2 lists all of the hyperfine parameters, namely the percentage of area, isomer shift (IS), hyperfine field (B_{hf}) and quadrupole splitting (QS). It

should also be noted that the Mössbauer results are consistent with the experimental evidence and the outcomes of the spectroscopic characterizations (XRD, FTIR, Raman and XPS).

To investigate the morphology and topology of the as-prepared $MFe_{12}O_{19}$ nanoparticles, SEM images were recorded for all $MFe_{12}O_{19}$ NPs (Fig. 7). $CuFe_{12}O_{19}$ shows a uniform nanostructure with a homogeneous shape distribution and slight agglomerations (Fig. 7a$_1$). However, $SnFe_{12}O_{19}$ reveals a slightly uniform distribution of crystallized NPs (Fig. 7b$_1$). On the other hand, $SrFe_{12}O_{19}$ shows the formation of nano-sized grains and uniform particle shape distribution (Fig. 7c$_1$). Moreover, all EDX elemental mapping images indicate that the main constituent elements of the synthesized $MFe_{12}O_{19}$ nanostructures are well-dispersed throughout the structure (Fig. 7a$_2$–c$_2$).

TEM analysis was performed to further investigate the shape and size of the as-synthesized $MFe_{12}O_{19}$ nanostructures (Fig. 8). The TEM images of $CuFe_{12}O_{19}$ reveal spherical nanoparticles with a size range of approximately 75–85 nm, and confirm the presence of tightly agglomerated NPs (Fig. 8a). The TEM images of $SnFe_{12}O_{19}$ reveal small platelets forming large spherical grains, with an average size of about 40–80 nm (Fig. 8b), while the TEM images of $SrFe_{12}O_{19}$ reveal interconnected spherical NPs with a size range of about 25–55 nm (Fig. 8c).

Fig. 9 shows the nitrogen adsorption–desorption isotherms of $CuFe_{12}O_{19}$, $SnFe_{12}O_{19}$ and $SrFe_{12}O_{19}$ NPs. According to the IUPAC classification, the isotherms of the $MFe_{12}O_{19}$ NPs may be assigned to type III, III and II for the $CuFe_{12}O_{19}$, $SnFe_{12}O_{19}$ and $SrFe_{12}O_{19}$ NPs, respectively. The pore size distributions (BJH model) of all $MFe_{12}O_{19}$ NPs are presented in the inset spectra in Fig. 9a–c. The BJH average pore diameters of $CuFe_{12}O_{19}$, $SnFe_{12}O_{19}$ and $SrFe_{12}O_{19}$ NPs are found to be 12.98, 14.95 and 4.89 nm, respectively. According to the IUPAC, these average values indicate that the as-synthesized $MFe_{12}O_{19}$ are classified as a mesoporous nanomaterial.[57,58] Moreover, the BET surface area of the obtained NPs was found to be 1.87, 5.25 and 24.91 m^2 g^{-1}, respectively.

To evaluate the stability of the as-prepared $MFe_{12}O_{19}$ for potential catalytic applications, zeta potential (ZP) measurements were carried out on $MFe_{12}O_{19}$ NPs dispersed in a solvent (acetonitrile; acetone or deionized water). The $CuFe_{12}O_{19}$, $SnFe_{12}O_{19}$ and $SrFe_{12}O_{19}$ NPs present ZP values of −24.8, −16.9

Table 2 Hyperfine parameters of the room temperature Mössbauer spectra of $CuFe_{12}O_{19}$, $SrFe_{12}O_{19}$ and $SnFe_{12}O_{19}$

$MFe_{12}O_{19}$	Component	Area (%)	IS (mm s^{-1})	B_{hf} (T)	QS (mm s^{-1})	Site
$CuFe_{12}O_{19} = \{CuFe_2O_4$–$Fe_2O_3\}$	Sextet-1	72.35	0.36	51.71	—	Octahedral
	Sextet-2	12.15	0.36	50.16	—	Tetrahedral
	Doublet	15.50	0.59	—	2.65	—
$SrFe_{12}O_{19}$	Sextet-1	25.12	0.28	51.95	—	4f2
	Sextet-2	7.00	0.39	50.93	—	2a
	Sextet-3	10.96	0.26	49.13	—	4f1
	Sextet-4	55.94	0.36	40.90	—	12k
	Sextet-5	0.98	0.38	34.95	—	2b
$SnFe_{12}O_{19} = \{SnO_2$–$Fe_2O_3\}$	Doublet	100	0.41	—	0.20	—
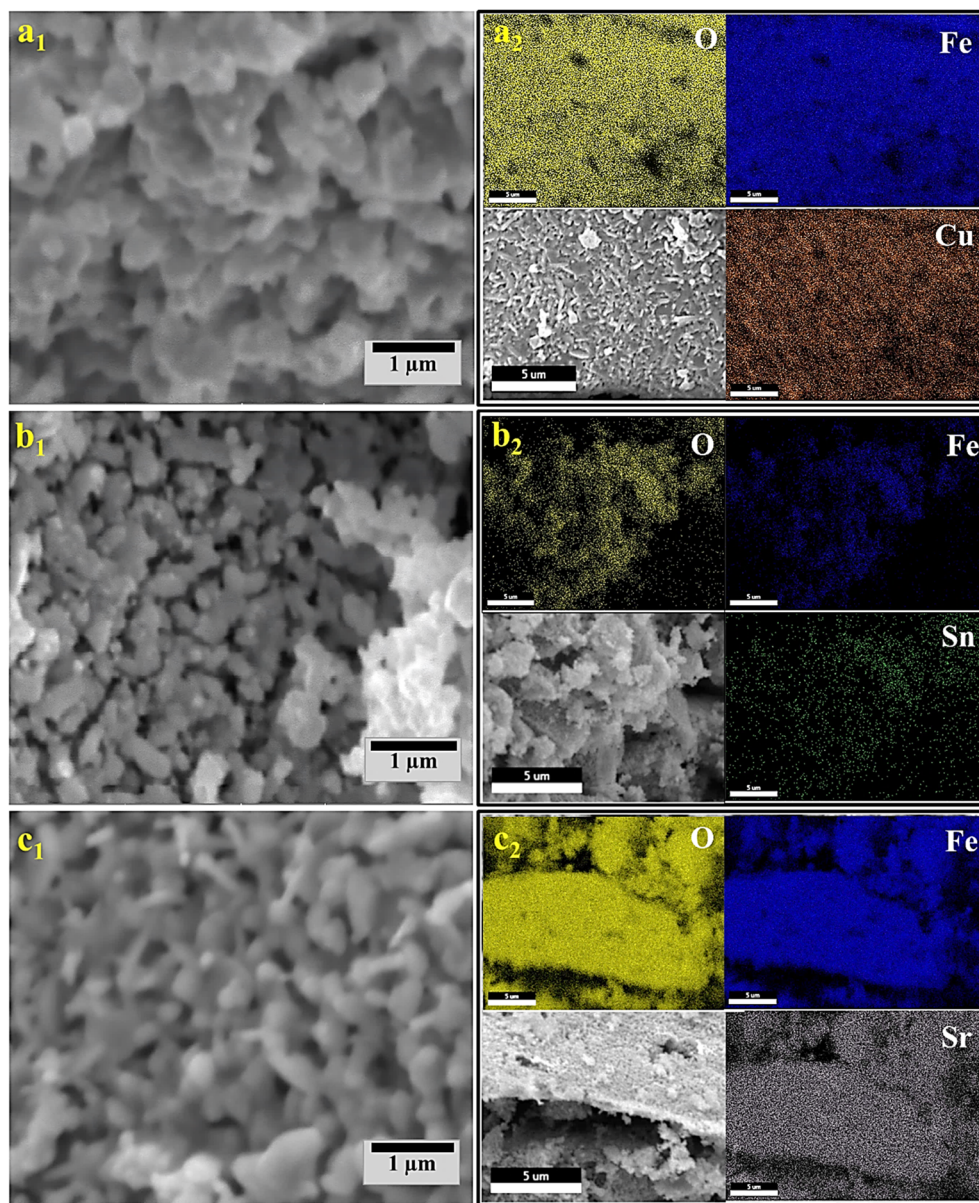
Fig. 7 SEM images and EDX elemental maps of (a) $CuFe_{12}O_{19}$, (b) $SnFe_{12}O_{19}$ and (c) $SrFe_{12}O_{19}$.

and −20.6 mV, respectively. Accordingly, it was reported that NPs manifesting −25 > ZP > +25 mV usually indicate a high degree of stability.[59] Indeed, the obtained surface charge values indicate that the prepared NPs exhibit stabilities ranging from good to a high degree of stability. In addition, the obtained ZP values of the synthesized $MFe_{12}O_{19}$ confirm the observed fluctuation in particle agglomeration (Cu > Sr > Sn) during the microscopic study ($CuFe_{12}O_{19}$ presents a threshold ZP value).

3.2. Catalytic studies

The catalytic activity of the as-synthesized $MFe_{12}O_{19}$ NPs were evaluated in the selective oxidation reaction of aromatic olefins. Hence, styrene was chosen as a model substrate to conduct the

optimization study of the catalytic oxidation. Moreover, preliminary catalytic tests of $MFe_{12}O_{19}$ were focused on the selective formation of styrene oxide or benzaldehyde, while tBHP or H_2O_2 were used as the oxidizing agent (Scheme 1 and Table 3).

In the absence of a catalyst, the oxidation reaction gives only a conversion of up to 8% (Table 3). However, the $CuFe_{12}O_{19}$ nanoparticles exhibited the highest efficiency and selectivity in the presence of both oxidizing agents (tBHP or H_2O_2). While the use of H_2O_2 in acetone provides a high selectivity towards benzaldehyde (80%) in the presence of $CuFe_{12}O_{19}$, switching to tBHP in acetonitrile resulted in two times higher selectivity towards styrene oxide formation (61%) compared to benzaldehyde (30%). Therefore, both reaction conditions (1 and 2) were optimized for a better catalytic selectivity throughout the study
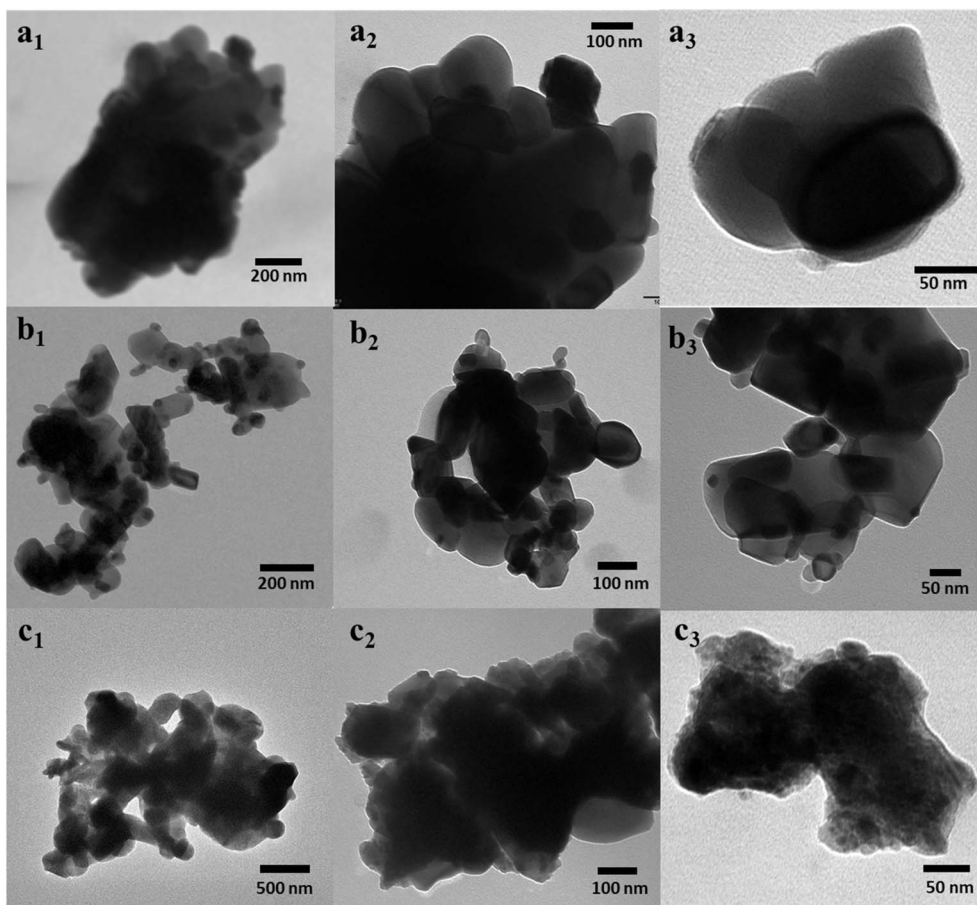
Fig. 8 TEM images of (a) $CuFe_{12}O_{19}$, (b) $SnFe_{12}O_{19}$ and (c) $SrFe_{12}O_{19}$.

of various parameters: the catalyst amount, reaction time, temperature, amount of oxidizing agent and solvent nature (Scheme 2).

To investigate the active site responsible for the obtained catalytic performance, we studied the catalytic activity of both $CuFe_2O_4$ and Fe_2O_3 compared to the as-prepared composite structure $CuFe_{12}O_{19}$ (Table 4). Indeed, the XRD pattern and Rietveld refinement of $CuFe_{12}O_{19}$ illustrate the presence of both $CuFe_2O_4$ and Fe_2O_3 phases as the composite nanostructure ($CuFe_{12}O_{19} = \{CuFe_2O_4-Fe_2O_3\}$ composite). Hence, the catalytic oxidation in the presence of $CuFe_{12}O_{19}$ reveals high conversion and good selectivity compared to $CuFe_2O_4$ or Fe_2O_3 for both reaction conditions. Consequently, the composite structure of the as-prepared $CuFe_{12}O_{19}$ NPs effectively enhances the catalytic activity and reusability of the developed nanocatalyst, owing to the synergistic catalytic effect in a single magnetically recoverable nanostructure.

3.3. Optimization of the $CuFe_{12}O_{19}$ catalyzed oxidation of styrene

3.3.1. Effect of solvent. An examination of the protic and aprotic solvents on the model reaction using $CuFe_{12}O_{19}$ as the catalyst and tBHP or H_2O_2 as the oxidizing agent has been

carried out (Table 5). On the one hand, the presence of tBHP in polar and aprotic solvents (acetonitrile, acetone and THF) promotes the selective formation of styrene oxide, compared to the protic ones. On the other hand, acetone provides the best selectivity towards benzaldehyde when using H_2O_2 as the oxidizing agent. For further optimizations, the catalytic oxidation will be carried out in the presence of tBHP in acetonitrile for the selective formation of epoxide (condition 1), while H_2O_2 in acetone will be used for the selective synthesis of aldehyde (condition 2).

3.3.2. Effect of the reaction temperature. Table 6 shows the effect of temperature on the selective catalytic oxidation of styrene in the presence of $CuFe_{12}O_{19}$ nanoparticles as the catalyst. In the presence of tBHP, the optimum conversion/ selectivity was obtained at 60 °C and the elevated temperature (80 °C) resulted in a decrease of the styrene oxide selectivity due to the epoxide ring-opening. Moreover, when the reaction was conducted in the presence of H_2O_2 as the oxidizing agent, the increase of temperature to 80 °C resulted in a total styrene conversion and a high selectivity towards benzaldehyde. Therefore, further optimization studies were conducted at 60 °C and 80 °C for conditions 1 and 2, respectively.

3.3.3. Effect of the catalyst amount. The selective catalytic oxidation of styrene was carried out in the presence of different
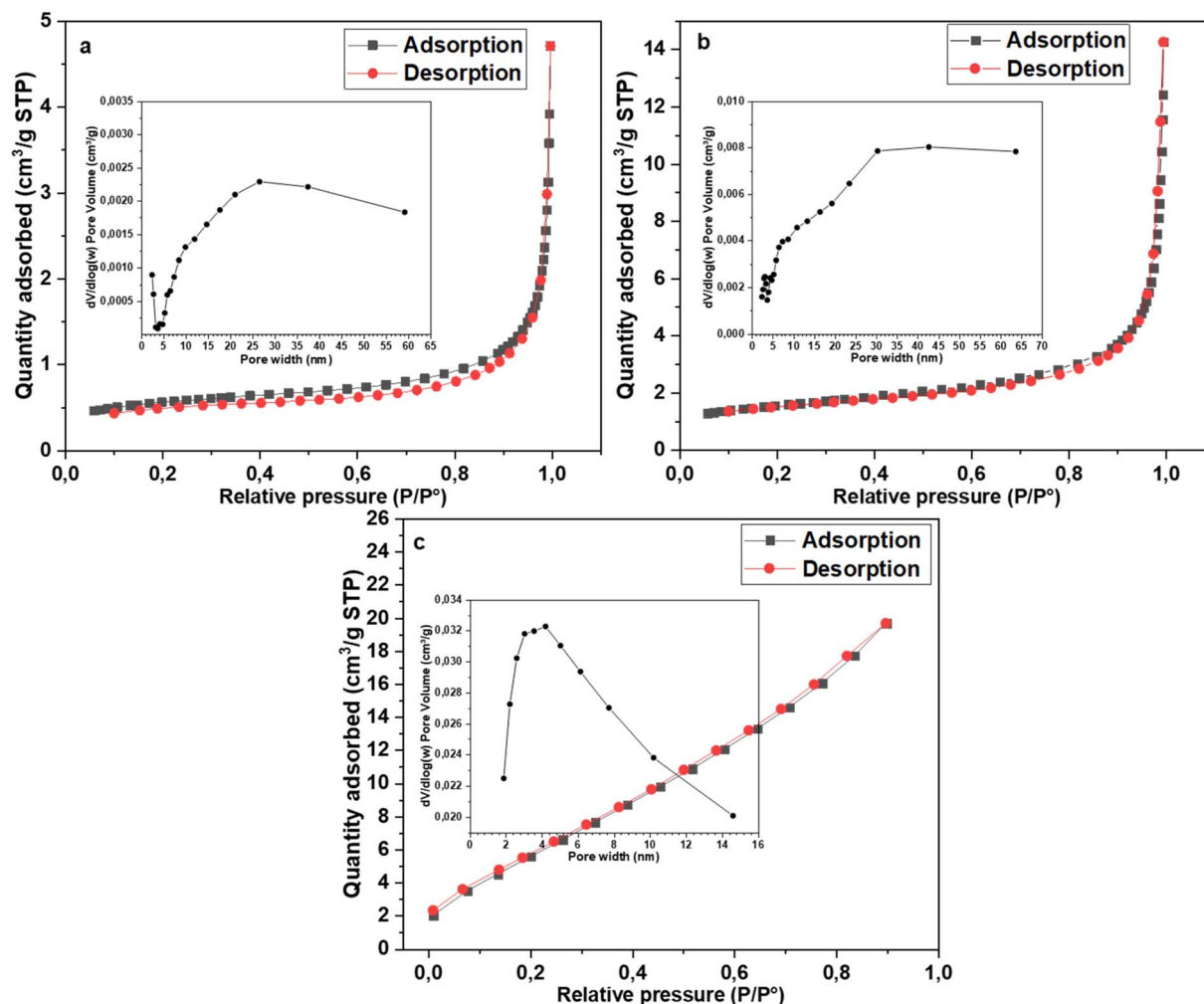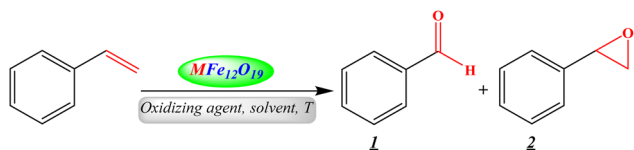
Fig. 9 N₂ adsorption–desorption isotherm and BJH pore diameter distribution of (a) CuFe₁₂O₁₉, (b) SnFe₁₂O₁₉ and (c) SrFe₁₂O₁₉.

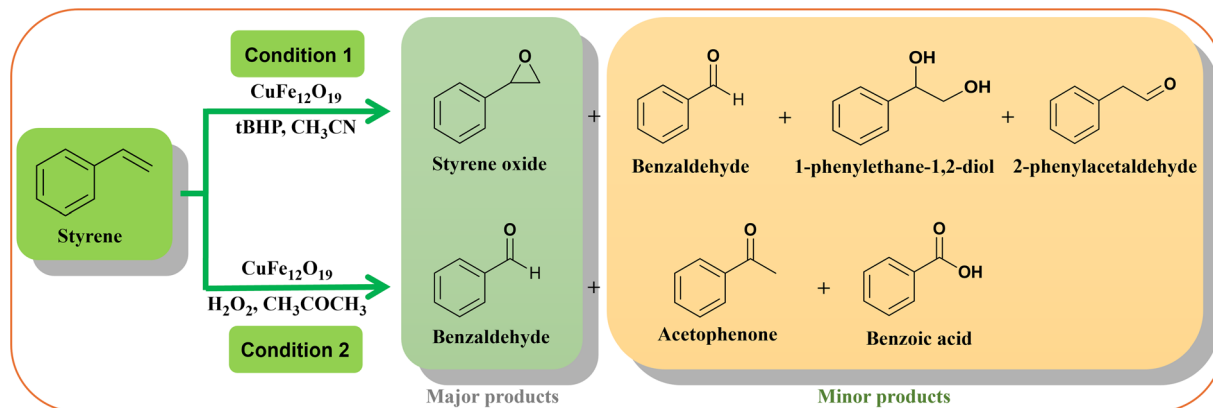
Scheme 1 Selective catalytic oxidation of styrene.

amounts of CuFe₁₂O₁₉ as the catalyst (Table 7). When the reaction was performed with *t*BHP as the oxidant, the best result was obtained with 20 mg of CuFe₁₂O₁₉, giving a selective formation of styrene oxide of 61%. Similarly, in the presence of H₂O₂, the optimal CuFe₁₂O₁₉ amount was 20 mg with a total conversion and a high selectivity of benzaldehyde of up to 81%.

Table 3 Catalytic oxidation^a of styrene in the presence of *t*-BHP^b or H₂O₂^c

Reaction	Catalyst	T (°C)	Ox. agent	Solvent	Conversion^d (%)	Yield^d (%)	
						Benzaldehyde	Styrene oxide
Condition 1	—	60	*t*BHP	Acetonitrile	8	7	—
	CuFe₁₂O₁₉	**60**	***t*BHP**	**Acetonitrile**	**93**	**30**	**61**
	SnFe₁₂O₁₉	60	*t*BHP	Acetonitrile	20	11	8
	SrFe₁₂O₁₉	60	*t*BHP	Acetonitrile	30	11	18
Condition 2	—	80	H₂O₂	Acetone	4	4	—
	CuFe₁₂O₁₉	**80**	**H₂O₂**	**Acetone**	**100**	**80**	—
	SnFe₁₂O₁₉	80	H₂O₂	Acetone	100	28	—
	SrFe₁₂O₁₉	80	H₂O₂	Acetone	72	40	—

^{a} General reaction conditions: 1.92 mmol of styrene with 3 eq. of oxidizing agent and 2 ml of solvent for 24 h. ^{b} Condition 1: *t*BHP in acetonitrile at 60 °C. ^{c} Condition 2: H₂O₂ in acetone at 80 °C. ^{d} The conversion and yields were determined by GC using dodecane as the internal standard.

Scheme 2 Catalytic oxidation of styrene in the presence of tBHP or H_2O_2.

Table 4 Comparison of the catalytic activity of the as-prepared nanomaterials in catalytic styrene oxidation[a]

			Yield[b] (%)	
Oxidizing agent	Catalyst	Conversion[b] (%)	Benzaldehyde	Styrene oxide
tBHP	Fe_2O_3	86	34	39
	$CuFe_2O_4$	99	14	37
	$CuFe_{12}O_{19}$	**93**	**30**	**61**
H_2O_2	Fe_2O_3	18	11	Trace
	$CuFe_2O_4$	5	Trace	—
	$CuFe_{12}O_{19}$	**100**	**81**	—

[a] General reaction conditions: 1.92 mmol of styrene, 3 eq. of oxidizing agent (tBHP, acetonitrile at 60 °C or H_2O_2, acetone at 80 °C), catalyst (20 mg) and 2 ml of solvent for 24 h. [b] The conversion and yields were determined by GC using dodecane as the internal standard.

Table 5 Effect of solvent on the styrene oxidation in the presence of $CuFe_{12}O_{19}$ NPs as the catalyst[a]

			Yield[b] (%)	
Oxidizing agent	Solvent	Conversion[b] (%)	Benzaldehyde	Styrene oxide
tBHP	None	24	6	17
	H_2O	17	16	—
	Methanol	45	26	13
	Ethanol	18	14	3
	Acetonitrile	**93**	**30**	**61**
	THF	65	19	43
	Acetone	63	17	39
H_2O_2	None	5	5	—
	H_2O	4	4	—
	Methanol	82	10	—
	Ethanol	100	17	—
	Acetonitrile	22	20	—
	THF	79	45	—
	Acetone	**100**	**81**	—

[a] General reaction conditions: 1.92 mmol of styrene, 3 eq. of oxidizing agent (tBHP at 60 °C or H_2O_2 at 80 °C), $CuFe_{12}O_{19}$ (20 mg) and 2 ml of solvent for 24 h. [b] The conversion and yields were determined by GC using dodecane as the internal standard.

Therefore, further optimization studies were conducted using 20 mg of catalyst.

3.3.4. Effect of oxidizing agent/styrene molar ratio. The selective catalytic oxidation of styrene was performed by varying the molar ratio of the oxidizing agent/styrene (Table 8). The increase of the tBHP/styrene molar ratio to 3 enhances both conversion and selectivity of styrene oxide. However, with a tBHP/styrene molar ratio of 4, the selectivity of styrene oxide decreases due to the formation of benzoic acid. Similarly, a H_2O_2/styrene molar ratio of 3 gave the best result.

Table 6 Effect of the reaction temperature on the styrene oxidation in the presence of $CuFe_{12}O_{19}$ NPs as the catalyst[a]

Reaction	Temperature (°C)	Conversion[d] (%)	Yield[d] (%)	
			Benzaldehyde	Styrene oxide
Condition 1[b]	50	64	20	40
	60	**93**	**30**	**61**
	70	100	32	59
	80	100	44	11
Condition 2[c]	50	23	21	—
	60	24	22	—
	70	52	50	—
	80	**100**	**81**	—

[a] General reaction conditions: 1.92 mmol of styrene with 3 eq. of oxidizing agent, $CuFe_{12}O_{19}$ (20 mg) and 2 ml of solvent for 24 h. [b] Condition 1: tBHP in acetonitrile. [c] Condition 2: H_2O_2 in acetone. [d] The conversion and yields were determined by GC using dodecane as the internal standard.

Table 7 Effect of the catalyst amount on the styrene oxidation in the presence of $CuFe_{12}O_{19}$ NPs as the catalysts[a]

Reaction	Catalyst amount (mg)	Conversion[d] (%)	Yield[d] (%)	
			Benzaldehyde	Styrene oxide
Condition 1[b]	10	87	33	51
	15	91	32	57
	20	**93**	**30**	**61**
	25	96	36	56
	30	85	33	51
Condition 2[c]	10	85	68	—
	15	88	70	—
	20	**100**	**81**	—
	25	100	67	—
	30	100	60	—

[a] General reaction conditions: 1.92 mmol of styrene with 3 eq. of oxidizing agent, $CuFe_{12}O_{19}$ and 2 ml of solvent for 24 h. [b] Condition 1: tBHP in acetonitrile at 60 °C. [c] Condition 2: H_2O_2 in acetone at 80 °C. [d] The conversion and yields were determined by GC using dodecane as the internal standard.

3.3.5. Effect of the reaction time. A kinetic study of the selective catalytic oxidation of styrene was carried out (Table 9). The evolution of the reaction *versus* time shows that styrene oxide or benzaldehyde were formed as major products in the presence of tBHP and H_2O_2, respectively. The best result was obtained within 24 h.

3.3.6. Effect of basicity. To improve the epoxide selectivity in the oxidation of olefins, the effect of the reaction medium basicity should be taken into consideration. Indeed, the selective catalytic oxidation of styrene-to-styrene oxide was performed using different amounts of urea to assess the effect of basicity (Fig. 10). In the presence of 20 mg of urea (17.34 mol%),

Table 8 Effect of the oxidizing agent/styrene molar ratio on the styrene oxidation in the presence of $CuFe_{12}O_{19}$ NPs as catalysts[a]

| Reaction	Oxidizing agent/styrene	Conversion[d] (%)	Yield[d] (%)	
			Benzaldehyde	Styrene oxide
Condition 1[b]	1	43	15	24
	2	66	19	42
	3	**93**	**30**	**61**
	4	80	30	45
Condition 2[c]	1	10	9	—
	2	40	26	—
	3	**100**	**81**	—
	4	100	48	—

[a] General reaction conditions: 1.92 mmol of styrene, oxidizing agent, $CuFe_{12}O_{19}$ (20 mg) and 2 ml of solvent for 24 h. [b] Condition 1: tBHP in acetonitrile at 60 °C. [c] Condition 2: H_2O_2 in acetone at 80 °C. [d] The conversion and yields were determined by GC using dodecane as the internal standard.

Table 9 Effect of the reaction time on the styrene oxidation in the presence of CuFe$_{12}$O$_{19}$ NPs as catalysts[a]

Reaction	Time (h)	Conversion[d] (%)	Yield[d] (%)	
			Benzaldehyde	Styrene oxide
Condition 1[b]	3	28	12	12
	6	48	20	21
	12	78	29	46
	15	83	30	50
	18	87	30	55
	24	**93**	**30**	**61**
Condition 2[c]	3	9	8	—
	6	40	36	—
	12	68	61	—
	15	77	67	—
	18	83	68	—
	24	**100**	**81**	—

[a] General reaction conditions: 1.92 mmol of styrene with 3 eq. of oxidizing agent, CuFe$_{12}$O$_{19}$ (20 mg) and 2 ml of solvent. [b] Condition 1: tBHP in acetonitrile at 60 °C. [c] Condition 2: H$_2$O$_2$ in acetone at 80 °C. [d] The conversion and yields were determined by GC using dodecane as the internal standard.
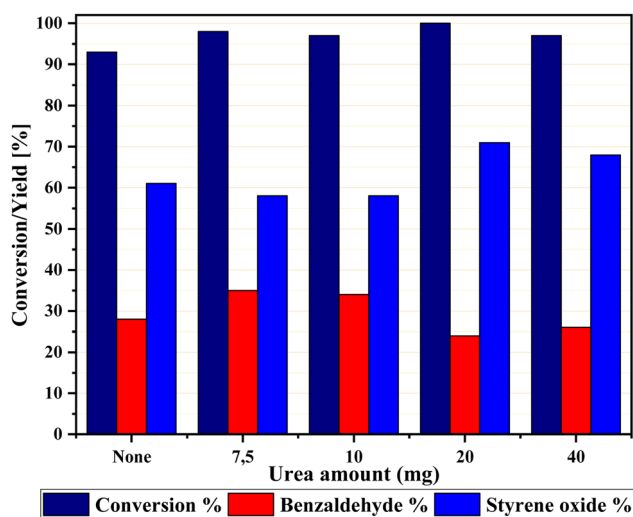
Fig. 10 Effect of urea in the presence of tBHP and CuFe$_{12}$O$_{19}$ as the catalyst.

a total conversion was obtained and the selectivity of styrene oxide increases to 72%. This result can be explained by the stabilization effect of urea on the epoxide function, which avoids the epoxide ring-opening *via* hydrolysis reaction. Indeed, Liu *et al.* have reported that the basicity of the solvent medium increases the styrene oxide selectivity.[17]

3.4. Heterogeneity test

A hot-filtration test was performed to investigate the heterogeneity of the CuFe$_{12}$O$_{19}$ NPs catalytic system (Fig. 11). After 12 h of the catalytic oxidation of styrene, the catalyst was separated from the reaction mixture by an external magnetic field and the obtained filtrate was continually stirred under the same reaction conditions. The results indicated that no significant enhancement of the styrene conversion was observed even after completing 24 h of reaction time. This result clearly indicates

that the CuFe$_{12}$O$_{19}$ nanoparticles act as a heterogeneous catalyst in the styrene oxidation.

3.5. Recycling of catalyst

Since catalyst recyclability has great potential for practical applications, the reusability of magnetic CuFe$_{12}$O$_{19}$ NPs was evaluated in five consecutive cycles in the selective styrene oxidation reaction under gram-scale conditions (Fig. 12). In the presence of tBHP, the catalytic activity of CuFe$_{12}$O$_{19}$ NPs slightly decreases in terms of the styrene conversion and styrene oxide selectivity during the consecutive runs. Hence, the investigation of XRD analysis shows that the identity of the recovered CuFe$_{12}$O$_{19}$ catalyst remains like the fresh one (Fig. 13a). However, the SEM image shows agglomerated particles with a change in the surface morphology (Fig. 13b), which could explain the noticeable drop in the reaction conversion and selectivity. On the other hand, the
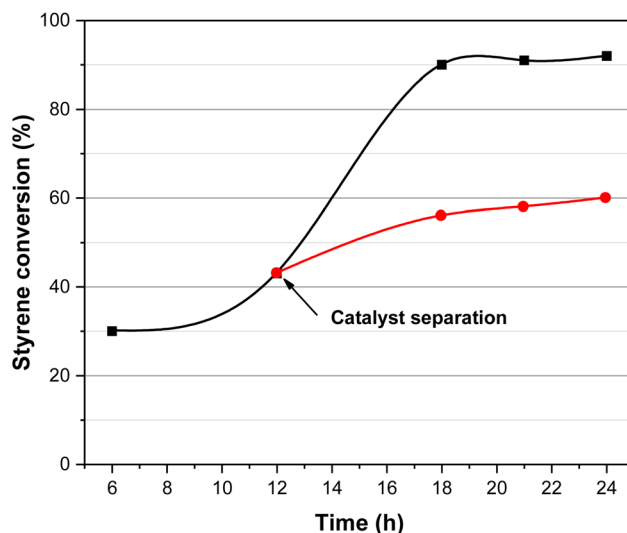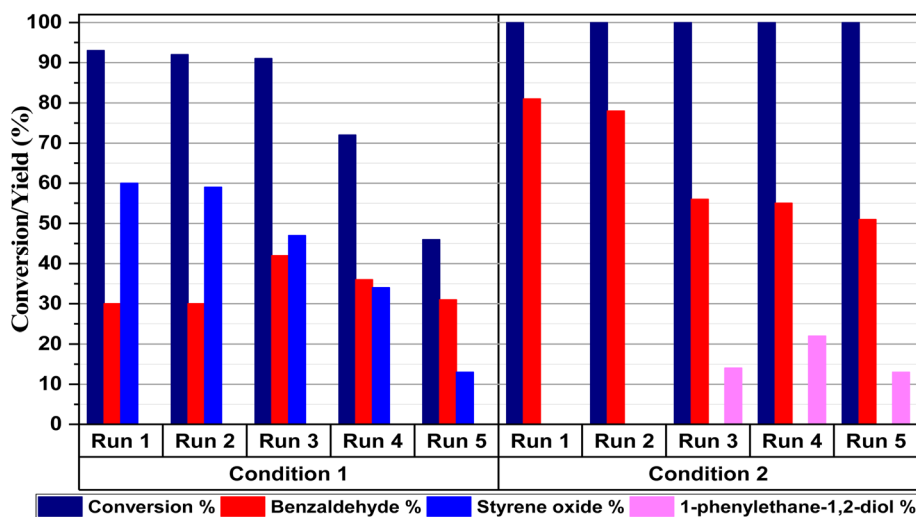

Fig. 11 Heterogeneity test of the CuFe$_{12}$O$_{19}$ nanoparticles.

© 2025 The Author(s). Published by the Royal Society of Chemistry

Fig. 12 $CuFe_{12}O_{19}$ reusability in the gram-scale selective catalytic oxidation of styrene.

selective catalytic reaction carried out in presence of H_2O_2 and $CuFe_{12}O_{19}$ exhibits a total and stable conversion within the five runs with a slight decrease in benzaldehyde selectivity over the runs. Furthermore, the XRD patterns and SEM images of the recycled $CuFe_{12}O_{19}$ catalyst present no obvious changes compared to the fresh one (Fig. 13a and c).

3.6. Catalytic oxidation of styrene derivatives

With the optimized reaction conditions (1 and 2) in hand, the scope and limitations of the as-developed catalytic system

$MFe_{12}O_{19}$ were investigated in the catalytic oxidation of various aromatic olefins in the presence of $CuFe_{12}O_{19}$ NPs as catalysts (Table 10). All studied olefins were selectively converted to the corresponding oxygenated products in excellent to good yields.

3.7. Comparison of the catalytic performance of MNPs

To shed more light on the scope of $CuFe_{12}O_{19}$ NPs in organic synthesis as MNPs catalysts, the catalytic performance of other MNPs-based catalysts that have been tested in styrene catalytic oxidation so far is summarized in Table 11. Compared to the
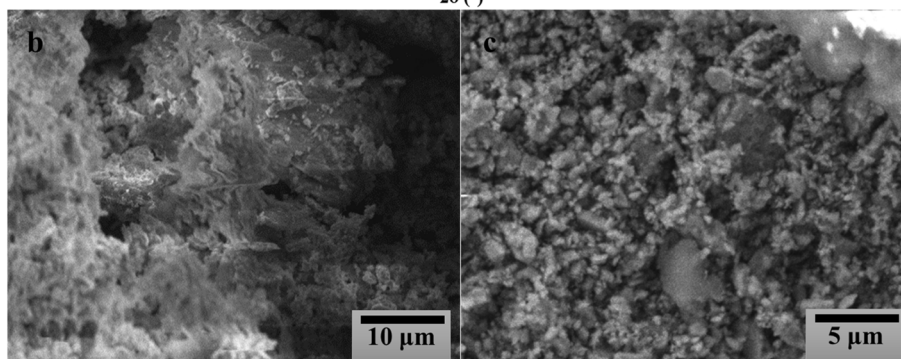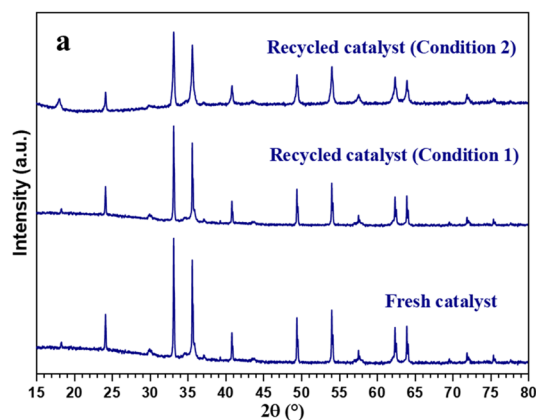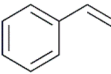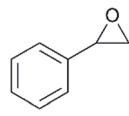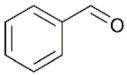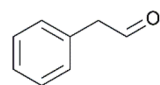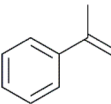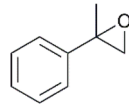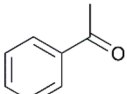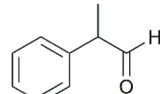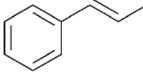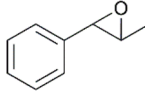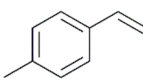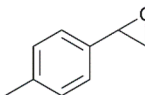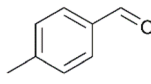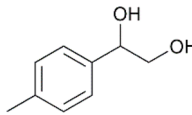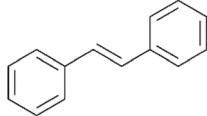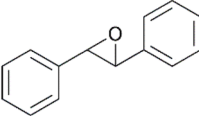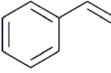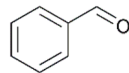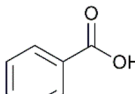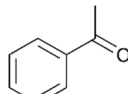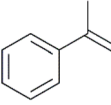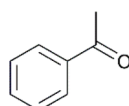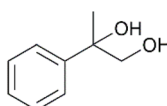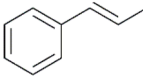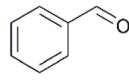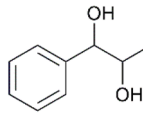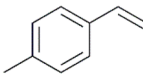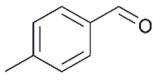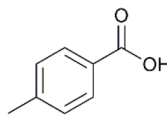
Fig. 13 XRD patterns of the fresh and recycled $CuFe_{12}O_{19}$ (a), and SEM images of $CuFe_{12}O_{19}$ after five runs while using (b) tBHP or (c) H_2O_2.

Table 10 Catalytic oxidation of styrene derivatives in presence of $CuFe_{12}O_{19}$ NPs as catalyst[a]

Reaction	Substrate	Conversion[d] (%)	Yield[d] (%)		
Condition 1[b]		100	72	24	Trace
		98	54	35	7
		100	93	—	—
		100	50	14	16
		80	75	—	—
Condition 2[c]		100	81	10	7
		71	60	9	—
		80	25	39	—
		58	45	Trace	—

[a] General reaction conditions: 1.92 mmol of styrene with 3 eq. of oxidizing agent, $CuFe_{12}O_{19}$ (20 mg) and 2 ml of solvent for 24 h. [b] Condition 1: tBHP in acetonitrile with 20 mg of urea at 60 °C. [c] Condition 2: H_2O_2 in acetone at 80 °C. [d] The conversion and yields were determined by GC using dodecane as the internal standard.

Table 11 Comparison of the catalytic activity of MNPs towards the selective oxidation of styrene

Catalyst		Ox. agent	Conv. (%)	Select. SO (%)	Select. BA (%)	Reusability (conv. % : run)	Ref.
$CoFe_2O_4$		tBHP	81	76	23	92 : 5	17
α-Fe_2O_3		tBHP	73	77	ND	—	60
$Au/_L$-Fe_3O_4		tBHP	76.1	70.1	27.5	—	61
Ag/KOH-γ-Fe_2O_3		tBHP	89.6	89.7	10.3	89 : 5	62
$MFe_{12}O_{19}$	**$CuFe_{12}O_{19}$= {$CuFe_2O_4$–Fe_2O_3}**	**tBHP**	**100**	**72**	**24**	**45 : 5**	**Present work**
	$SnFe_{12}O_{19}$= {SnO_2–Fe_2O_3}	**tBHP**	**65**	**26**	**5**	**—**	
	$SrFe_{12}O_{19}$	**tBHP**	**30**	**11**	**18**	**—**	
$SrFe_2O_4$		H_2O_2	63.7	ND	32	42 : 2	20
$BaFe_2O_4$		H_2O_2	45.1	9.5	88.5	31 : 3	63
$CaFe_2O_4$		H_2O_2	37.9	ND	91.1	—	64
$NiFe_2O_4$		H_2O_2	31.4	ND	55.6	—	18
$MFe_{12}O_{19}$	**$CuFe_{12}O_{19}$= {$CuFe_2O_4$–Fe_2O_3}**	**H_2O_2**	**100**	**—**	**82**	**100 : 5**	**Present work**
	$SnFe_{12}O_{19}$= {SnO_2–Fe_2O_3}	**H_2O_2**	**100**	**—**	**28**	**—**	
	$SrFe_{12}O_{19}$	**H_2O_2**	**72**	**—**	**40**	**—**	

previous studies, $CuFe_{12}O_{19}$ exhibits a high catalytic conversion with good selectivity under both conditions (1 and 2). The higher efficiency of $CuFe_{12}O_{19}$ MNPs can be attributed to the superior catalytic role of Cu and its synergistic effect with Fe, in comparison to Sn and Sr in the studied $MFe_{12}O_{19}$ NPs. This can be explained by the synergy between $CuFe_2O_4$ and Fe_2O_3 during the oxidation process, where both Cu and Fe are involved in the coordination with the activated oxidizing agent (tBHP or H_2O_2). This could lead to the formation of peroxo or superoxo species, such as $Fe(III)OO^•$ and $Cu(II)OO^•$, complexes that may not be formed with Sn and Sr. Additionally, the possible synergistic intersection between Cu^+/Cu^{2+} and Fe^{2+}/Fe^{3+} redox pairs at the catalyst surface could also contribute to the observed catalytic performance.

4. Conclusion

Magnetically separable $MFe_{12}O_{19}$ NPs were successfully synthesized using the coprecipitation method. As-prepared $MFe_{12}O_{19}$ (M = Cu, Sn and Sr) NPs exhibited nanoscale particle size, magnetic behavior, mesoporous structure and good recyclability. Advanced characterization studies revealed that $SnFe_{12}O_{19}$ and $CuFe_{12}O_{19}$ are not isostructural with the $SrFe_{12}O_{19}$ M-type hexaferrite, due to confirmed coexistence of SnO_2–Fe_2O_3 and $CuFe_2O_4$–Fe_2O_3 as a composite structure, respectively. The magnetic $MFe_{12}O_{19}$ nanocatalysts were found to be highly efficient for the selective oxidation reaction of various styrene derivatives compared to other reported MNPs heterogeneous catalysts. Among the as-synthesized $MFe_{12}O_{19}$ NPs, $CuFe_{12}O_{19}$ was found to be the best catalyst either in the presence of tBHP or H_2O_2 as the oxidizing agent. The high catalytic activity and good selectivity of $CuFe_{12}O_{19}$ MNPs could be associated with the synergistic catalytic effect of $CuFe_2O_4$ and Fe_2O_3 in a single magnetically recoverable nanostructure, compared to $SnFe_{12}O_{19}$ and $SrFe_{12}O_{19}$. We can assume that the developed $MFe_{12}O_{19}$ MNPs present a facile and greener approach using magnetically recyclable nanostructures for the selective catalytic oxidation reaction of olefins.

Data availability

The device types used for recording spectra and other analytical data that support the findings of this study are included in the manuscript.

Conflicts of interest

The authors declare that they have no conflicts of interest.

References

1 N. Ma, Y. Yue, W. Hua and Z. Gao, *Appl. Catal., A*, 2003, **251**, 39–47.
2 J. Liu, F. Wang, Z. Gu and X. Xu, *Chem. Eng. J.*, 2009, **151**, 319–323.
3 S. Tian, C. Peng, J. Dong, Q. Xu, Z. Chen, D. Zhai, Y. Wang, L. Gu, P. Hu, H. Duan, D. Wang and Y. Li, *ACS Catal.*, 2021, **11**, 4946–4954.
4 A. Aberkouks, A. A. Mekkaoui, B. Boualy, S. El Houssame, M. Ait Ali and L. El Firdoussi, *Adv. Mater. Sci. Eng.*, 2018, **2018**, 2716435.
5 G. Grigoropoulou, J. H. Clark and J. A. Elings, *Green Chem.*, 2003, **5**, 1–7.
6 A. Patel and S. Pathan, *Ind. Eng. Chem. Res.*, 2012, **51**, 732–740.
7 C. M. Granadeiro, A. D. S. Barbosa, S. Ribeiro, I. C. M. S. Santos, B. De Castro, L. Cunha-Silva and S. S. Balula, *Catal. Sci. Technol.*, 2014, **4**, 1416–1425.
8 T. A. G. Duarte, I. C. M. S. Santos, M. M. Q. Simões, M. G. P. M. S. Neves, A. M. V. Cavaleiro and J. A. S. Cavaleiro, *Catal. Lett.*, 2014, **144**, 104–111.
9 S. S. Balula, L. Cunha-Silva, I. C. M. S. Santos, A. C. Estrada, A. C. Fernandes, J. A. S. Cavaleiro, J. Pires, C. Freire and A. M. V. Cavaleiro, *New J. Chem.*, 2013, **37**, 2341–2350.
10 A. Aberkouks, A. A. Mekkaoui, B. Boualy, S. E. L. Houssame, M. Ait Ali and L. El Firdoussi, *Mater. Today: Proc.*, 2019, **13**, 453–457.

11 V. R. Choudhary, R. Jha and P. Jana, *Catal. Commun.*, 2008, **10**, 205–207.

12 I. W. Davies, L. Matty, D. L. Hughes and P. J. Reider, *J. Am. Chem. Soc.*, 2001, **123**, 10139–10140.

13 M. Nemanashi and R. Meijboom, *Catal. Lett.*, 2013, **143**, 324–332.

14 D. Yin, L. Qin, J. Liu, C. Li and Y. Jin, *J. Mol. Catal. A:Chem.*, 2005, **240**, 40–48.

15 A. Aberkouks, A. A. Mekkaoui, M. Ait Ali, L. El Firdoussi and S. El Houssame, *J. Chem.*, 2020, **2020**, 1241952.

16 I. T. Horváth and P. T. Anastas, *Chem. Rev.*, 2007, **107**, 2167–2168.

17 J. Liu, R. Meng, J. Li, P. Jian, L. Wang and R. Jian, *Appl. Catal., B*, 2019, **254**, 214–222.

18 D. Guin, B. Baruwati and S. V. Manorama, *J. Mol. Catal. A:Chem.*, 2005, **242**, 26–31.

19 R. Ramanathan and S. Sugunan, *Catal. Commun.*, 2007, **8**, 1521–1526.

20 S. K. Pardeshi and R. Y. Pawar, *J. Mol. Catal. A:Chem.*, 2011, **334**, 35–43.

21 Ü. Özgür, Y. Alivov and H. Morkoç, *J. Mater. Sci.: Mater. Electron.*, 2009, **20**, 789–834.

22 J. M. D. Coey, *J. Alloys Compd.*, 2001, **326**, 2–6.

23 P. E. Kazin, L. A. Trusov, D. D. Zaitsev, Y. D. Tretyakov and M. Jansen, *J. Magn. Magn. Mater.*, 2008, **320**, 1068–1072.

24 A. Morisako, T. Naka, K. Ito, A. Takizawa, M. Matsumoto and Y. K. Hong, *J. Magn. Magn. Mater.*, 2002, **242–245**, 304–310.

25 P. Hernández, C. De Francisco, J. M. Muñoz, J. Iñiguez, L. Torres and M. Zazo, *J. Magn. Magn. Mater.*, 1996, **157–158**, 123–124.

26 Z. Jin, W. Tang, J. Zhang, H. Lin and Y. Du, *J. Magn. Magn. Mater.*, 1998, **182**, 231–237.

27 M. J. Iqbal, M. N. Ashiq, P. Hernandez-Gomez and J. M. Munoz, *J. Magn. Magn. Mater.*, 2008, **320**, 881–886.

28 B. T. Shirk and W. R. Buessem, *J. Am. Ceram. Soc.*, 1970, **53**, 192–196.

29 E. Alimohammadi, S. Sheibani and A. Ataie, *Mater. Chem. Phys.*, 2022, **275**, 125312.

30 R. C. Pullar, *Prog. Mater. Sci.*, 2012, **57**, 1191–1334.

31 F. Ansari, A. Sobhani and M. Salavati-Niasari, *J. Magn. Magn. Mater.*, 2016, **401**, 362–369.

32 A. Khoobi, M. Salavati-Niasari and O. Amiri, *J. Alloys Compd.*, 2021, **858**, 157745.

33 M. Laayati, A. Hasnaoui, N. Abdallah, S. Oubaassine, L. Fkhar, O. Mounkachi, S. El Houssame, M. Ait Ali and L. El Firdoussi, *J. Chem.*, 2020, 1–10.

34 M. Laayati, A. A. Mekkaoui, L. Fkhar, M. Ait Ali, H. Anane, L. Bahsis, L. El Firdoussi and S. El Houssame, *RSC Adv.*, 2022, **12**, 11139–11154.

35 Z. kheilkordi, G. Mohammadi Ziarani, S. Bahar and A. Badiei, *J. Iran. Chem. Soc.*, 2019, **16**, 365–372.

36 T. Ahmadi, G. Mohammadi Ziarani, S. M. Masoumian Hoseini, A. Badiei and M. M. Ranjbar, *J. Iran. Chem. Soc.*, 2021, **18**, 2047–2056.

37 F. Sanatkar, A. Khoobi and M. Salavati-Niasari, *Environ. Sci. Pollut. Res.*, 2021, **28**, 10791–10803.

38 M. Mahdiani, F. Soofivand, F. Ansari and M. Salavati-Niasari, *J. Cleaner Prod.*, 2018, **176**, 1185–1197.

39 P. C. A. Brito, R. F. Gomes, J. G. S. Duque and M. A. Macêdo, *Phys. B Condens. Matter*, 2006, **384**, 91–93.

40 A. Ghasemi and A. Morisako, *J. Magn. Magn. Mater.*, 2008, **320**, 1167–1172.

41 T. Chin, S. L. Hsu and M. C. Deng, *J. Magn. Magn. Mater.*, 1993, **120**, 64–68.

42 P. Sivakumar, L. Shani, Y. Yeshurun, A. Shaulov and A. Gedanken, *J. Mater. Sci.: Mater. Electron.*, 2016, **27**, 5707–5714.

43 Z. F. Zi, Y. P. Sun, X. B. Zhu, Z. R. Yang, J. M. Dai and W. H. Song, *J. Magn. Magn. Mater.*, 2008, **320**, 2746–2751.

44 R. A. Brand, *Normos Program, Internal Report, Angewandte Physic*, Univertitat Duisburg, 1987.

45 S. Wang, D. Li, Y. Xiao, W. Dang and J. Feng, *Russ. J. Phys. Chem. A*, 2017, **91**, 1981–1986.

46 M. A. P. Buzinaro, M. A. Macêdo, B. F. O. Costa and N. S. Ferreira, *Ceram. Int.*, 2019, **45**, 13571–13574.

47 J. Didari and A. Sadeghzadeh-Attar, *J. Taiwan Inst. Chem. Eng.*, 2021, **119**, 232–244.

48 T. P. Martin, R. Merlin, D. R. Huffman and M. Cardona, *Solid State Commun.*, 1977, **22**, 565–567.

49 N. Yang, H. Yang, J. Jia and X. Pang, *J. Alloys Compd.*, 2007, **438**, 263–267.

50 M. S. Chen, Z. X. Shen, X. Y. Liu and J. Wang, *J. Mater. Res.*, 2000, **15**, 483–487.

51 C. Akshhayya, M. K. Okla, A. A. Al-ghamdi, S. A. Al-amri, A. A. Alatar, M. A. Abdel-Maksoud, M. Aufy and S. S. Khan, *J. Cluster Sci.*, 2023, **34**, 2459–2469.

52 J. Li, X. Zhang, Y. Chen, Y. Li, Y. Huang, Z. Du and T. Li, *Chin. Sci. Bull.*, 2005, **50**, 1044–1047.

53 S. Katlakunta, S. Singh, S. Srinath, M. Bououdina, R. Sandhya and K. Praveena, *Mater. Res. Bull.*, 2015, **63**, 58–66.

54 M. Manikandan, K. S. Kumar, N. Aparnadevi and C. Venkateswaran, *Phys. Status Solidi A*, 2015, **212**, 2179–2185.

55 F. Zan, N. Jabeen, W. Xiong, A. Hussain, Y. Wang and H. Xia, *Nanotechnology*, 2020, **31**, 185402.

56 T. Xie, L. Xu, C. Liu and Y. Wang, *Appl. Surf. Sci.*, 2018, **273**, 684–691.

57 B. D. Zdravkov, J. J. Čermák, M. Šefara and J. Janků, *Cent. Eur. J. Chem.*, 2007, **5**, 385–395.

58 S. Polarz and B. Smarsly, *J. Nanosci. Nanotechnol.*, 2002, **2**, 581–612.

59 A. J. Shnoudeh, I. Hamad, R. W. Abdo, L. Qadumii, A. Y. Jaber, H. S. Surchi and S. Z. Alkelany, *Biomater. Bionanotechnol.*, 2019, 527–612.

60 R. A. Bepari, P. Bharali and B. K. Das, *J. Saudi Chem. Soc.*, 2017, **21**, S170–S178.

61 C. Huang, H. Zhang, Z. Sun, Y. Zhao, S. Chen, R. Tao and Z. Liu, *J. Colloid Interface Sci.*, 2011, **364**, 298–303.

62 Z. Pan, L. Hua, Y. Qiao, H. Yang, X. Zhao, B. Feng, W. Zhu and Z. Hou, *Chin. J. Catal.*, 2011, **32**, 428–435.

63 R. Y. Pawar and S. K. Pardeshi, *Arabian J. Chem.*, 2018, **11**, 282–290.

64 S. K. Pardeshi and R. Y. Pawar, *Mater. Res. Bull.*, 2010, **45**, 609–615.